A New Terrain-Following Vertical Coordinate Formulation for Atmospheric Prediction Models

Christoph Schär

Institute for Atmospheric and Climate Science, ETH, Zurich, Switzerland

Daniel Leuenberger

MeteoSwiss, Zurich, Switzerland

Oliver Fuhrer and Daniel Lüthi

Institute for Atmospheric and Climate Science, ETH, Zurich, Switzerland

Claude Girard

Recherche en Prévision Numérique, Environment Canada, Dorval, Quebec, Canada

ABSTRACT

Most numerical weather prediction models rely on a terrain-following coordinate framework. The computational mesh is thus characterized by inhomogeneities with scales determined by the underlying topography. Such inhomogeneities may affect the truncation error of numerical schemes. In this study, a new class of terrain-following coordinate systems for use in atmospheric prediction models is proposed. Unlike conventional systems, the new smooth level vertical (SLEVE) coordinate yields smooth coordinates at mid- and upper levels. The basic concept of the new coordinate is to employ a scale-dependent vertical decay of underlying terrain features. The decay rate is selected such that small-scale topographic variations decay much faster with height than their large-scale counterparts. This generalization implies a nonlocal coordinate transformation. The new coordinate is tested and compared against standard sigma and hybrid coordinate systems using an idealized advection test. It is demonstrated that the presence of coordinate transformations induces substantial truncation errors. These are critical for grid inhomogeneities with wavelengths smaller than approximately eight grid increments, and may overpower the regular-grid truncation error of the underlying finite-difference approximation. These results are confirmed by a theoretical analysis of the truncation error. In addition, the new coordinate is tested in idealized and real-case numerical experiments using a nonhydrostatic model. The simulations using the new coordinate yield a substantial reduction of small-scale noise in dynamical and thermodynamical model fields.

1. Introduction

Most numerical weather prediction (NWP) models employ some kind of terrain-following vertical coordinate system (e.g., Phillips 1957; Gal-Chen and Sommerville 1975; Simmons and Burridge 1981; Zhu et al. 1992; Webster et al. 1999). Such coordinates provide several important advantages: First, they map the atmospheric domain under consideration upon a rectangular computational mesh whose data structure is well suited for implementation on digital computers. Second, as the transformed vertical wind in computational space vanishes on the level of the topography, terrain-following coordinate transformations yield a simplification of the lower boundary condition. Third, as the approach allows for an unequal spacing of computational levels, it provides an easy method to couple the dynamical part of atmospheric prediction models with boundary and surface-layer parameterization schemes.

Despite these attractive properties, the introduction of terrain-following coordinates also implies serious disadvantages. Early research in this area relates to the detrimental impact of terrain-following coordinates upon the numerical formulation of the horizontal pressure gradient term (e.g., Janjić 1989). More recently, Klemp et al. (2002, manuscript submitted to *Mon. Wea. Rev.,* hereafter KSF). Used linear theory to analyze the role of terrain-following transformations on gravity wave generation and propagation. They demonstrate the

Corresponding author address: Christoph Schär, Institute for Atmospheric and Climate Science, Winterthurerstr. 190, 8057 Zürich, Switzerland.
E-mail: schaer@geo.umnw.ethz.ch

importance of a consistent numerical treatment of horizontal and vertical terms of the advection equation. The respective consistency assures that the appropriate numerical cancellations take place when differencing the fields on sloping coordinate surfaces. Lack of this cancellation leads to spurious small-scale forcing and may inflict significant distortions of the true solution, even for small-amplitude topography.

As an alternative to terrain-following transformations, coordinates with horizontal or quasi-horizontal computational surfaces have also been proposed. The potential usefulness of this approach in representing orographic blocking has been recognized for some time (Egger 1972), and a complete implementation in hydrostatic form has been realized by Mesinger et al. (1988). This quasi-horizontal coordinate is successful in avoiding horizontal pressure gradient errors on the synoptic scale, but the formulation has difficulties in representing flow over mesoscale topography (Gallus and Klemp 2000) and appears to be ill suited for high-resolution prediction models. Alternative formulations of z coordinates using shaved cells have also been proposed (Adcroft et al. 1997) and produce excellent results for some mesoscale adiabatic flows (Bonaventura 2000). However, the implementation of such coordinates in NWP models will require major modifications to parameterization packages.

Irrespective of the coordinate formulation under consideration, numerical solutions to orographic flow problems will deteriorate as the horizontal grid increment approaches the scales of the represented topographic features. A systematic analysis of Davies and Brown (2001) for dry flows demonstrates that the underrepresentation of orographic features will result in a substantial underestimation of the orographic drag, and experience with moist flows demonstrates that spurious precipitation may result from underresolved topography (Steppeler et al. 2001, hereafter SMAP). In order to circumnavigate these limitations, the digital topography used in operational NWP models is usually subjected to digital filtering. However, removing the whole range of underresolved terrain features would substantially reduce the height of topographic barriers and thereby inflict an underestimation of orographic blocking effects.

Comparatively little research has been carried out to evaluate the performance of classical numerical algorithms in the presence of terrain-following coordinate transformations. For instance, there is an extensive body of literature on properties of advection schemes in the presence of small-scale anomalies and regular grids, and this information is usually consulted when a scheme is evaluated for implementation in an atmospheric model. Yet the behavior of the same schemes in the presence of coordinate transformations has not been thoroughly investigated. Indeed, as will be shown in this paper, truncation errors inflicted by small-scale topographic features may become highly relevant.

The purpose of this study is twofold. First, we will investigate how various coordinate formulations behave in an idealized advection test. The test involves the horizontal advection of large-scale anomalies over an obstacle containing small-scale topographic features. It will be demonstrated that the truncation errors associated with standard coordinate transformations are critical and may, in fact, overpower the classical regular-grid truncation error of the underlying finite-difference approximation. Second, a new vertical coordinate formulation is proposed. This formulation allows the generation of a much smoother computational mesh and, thereby, drastically reduces the transformation errors referred to above. The key idea in generating this smooth coordinate is to adopt a scale-dependent decay with height of underlying terrain features. In essence, small-scale features are assigned fast decay rates, such that their signatures almost or completely disappear at upper levels. Well-resolved terrain features, on the other hand, do not pose a problem to numerical schemes and are allowed to decay much more slowly. The new coordinate will be referred to as smooth level vertical (SLEVE) coordinate.

The issue of small-scale topography and associated grid transformations is likely to gain importance in the near future, due to the continued increase in horizontal resolution of operational weather prediction and climate models (e.g., Benoit et al. 2002). For illustration, Fig. 1 displays a vertical cross section across the Alps at a horizontal resolution of 1 km. The diagrams to the left and right show the whole depth of the domain and its lower portion, respectively. Three coordinate formulations are considered. The classical sigma formulation (Figs. 1a,b) yields a very rough grid. Individual terrain features and mountain peaks are well visible in the coordinate surfaces, even at tropopause level. The use of hybrid coordinates (Figs. 1c,d) reduces the amplitude of these features, but not their presence itself. Only the new SLEVE coordinate formulation yields a smooth grid at midtropospheric levels (Figs. 1e,f).

We begin in section 2 by presenting the mathematical background and by providing the formulation of the new vertical coordinate transformation. Section 3 is devoted to a simplified advection test. The performance of several finite-difference schemes will be investigated using the three terrain-following coordinate transformations depicted in Fig. 1. In section 4, a theoretical analysis is presented of the truncation error's behavior in the presence of coordinate transformations. Section 5 finally discusses idealized and real-case numerical experiments using a nonhydrostatic numerical model. The study will be concluded in section 6.

2. Coordinate definition

a. Preliminaries

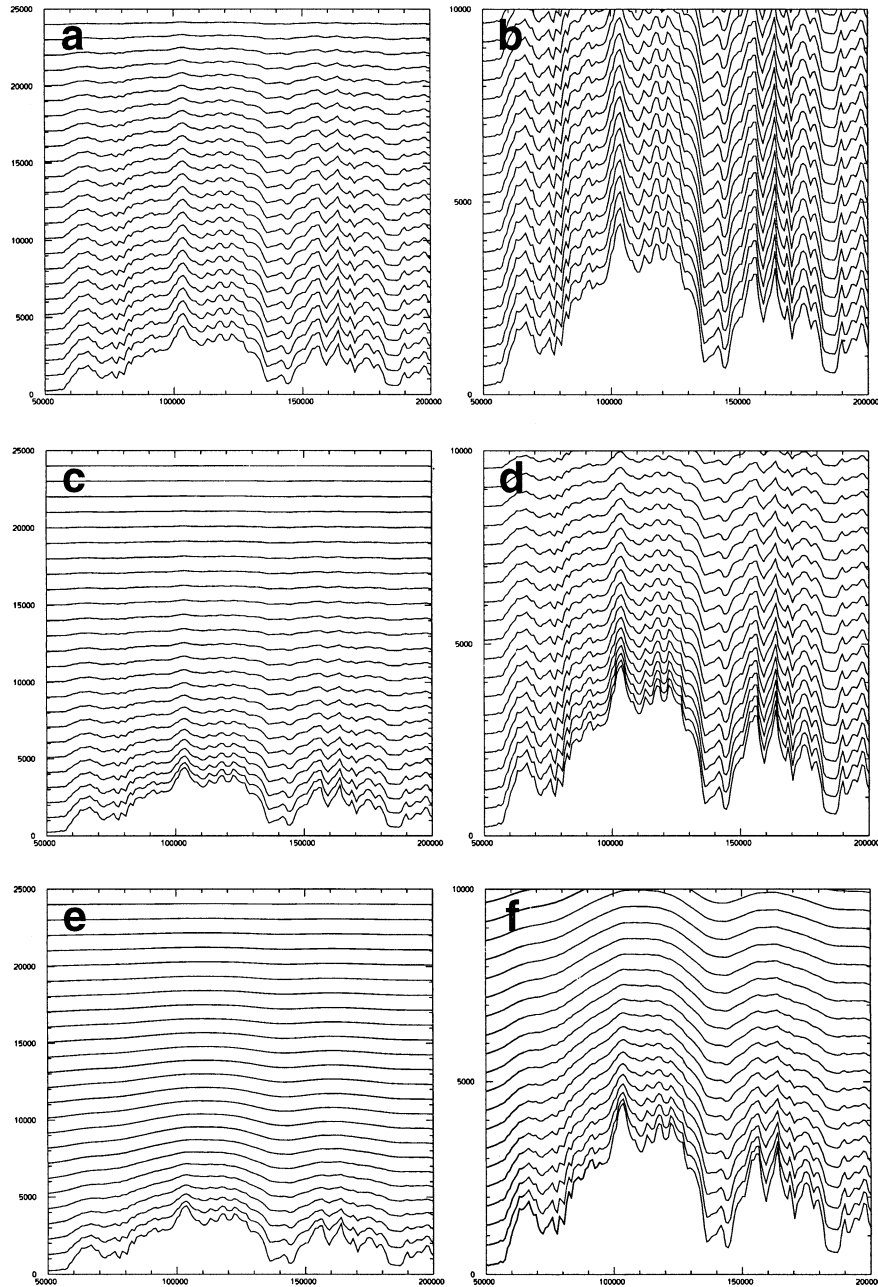We consider a Cartesian computational domain

FIG. 1. Vertical cross section showing three distributions of vertical coordinates. Left-hand panels show the full model depth (H = 25 km) with a coordinate spacing of Δx = 1 km; right-hand panels zoom into the lowermost 10 km with a coordinate spacing of 500 m. The three coordinates depict (a),(b) the sigma coordinate, (c),(d) a hybrid coordinate, and (e),(f) a SLEVE coordinate with a scale-dependent vertical decay of terrain features. The domain has a length of 150 km, a resolution of Δz = 1 km, and shows the Alpine topography at 7.87°E extending from the Po valley over the Monte Rosa massif and the Bernese Alps to the Rhine (from left to right). The coordinate formulation in (c),(d) is based upon (11) with s = 6 km, and in (e),(f) it is based upon (14) with s_1 = 10 km, s_2 = 2 km.

$$x_{\min} \leq x \leq x_{\max}, \qquad y_{\min} \leq y \leq y_{\max},$$

$$h(x, y) \leq z \leq H, \qquad (1)$$

that is confined below and above by the topographic height $h(x, y)$ and an upper lid at height H, respectively.

Generalized vertical coordinates may then be defined by a coordinate transformation of the form

$$Z = Z(x, y, z). \qquad (2)$$

Gal-Chen and Sommerville (1975) discuss two neces-

sary conditions for terrain-following coordinates: First, the transformation must map the computational domain (1) onto a rectangular domain in (x, y, Z) space. This requirement is met by imposing the boundary conditions

$$Z[x, y, h(x, y)] = 0 \quad \text{and} \quad Z(x, y, H) = H. \quad (3)$$

Second, the transformation must be invertible, so that the inverse transformation $z = z(x, y, Z)$ exists. This requires $Z(z)$ to be a strictly monotone function; that is,

$$J = \frac{\partial Z}{\partial z} > 0, \quad (4)$$

where J denotes the Jacobian of the transformation.

b. Vertical decay functions

To describe the vertical decay of terrain features with height, most atmospheric models use either one of two approaches. The first was proposed by Gal-Chen and Sommerville (1975) who investigated a specific transformation given by

$$Z(x, y, z) = H\frac{z - h(x, y)}{H - h(x, y)} \quad \text{or} \quad (5)$$

$$z(x, y, Z) = h(x, y) + Z[H - h(x, y)]/H. \quad (6)$$

This transformation, referred to as sigma coordinates, is particularly simple and implies a linear decay of the terrain features with height, while the Jacobian of the underlying transformation is independent of height; that is, $\partial J/\partial Z = 0$.

The second approach is based on Simmons and Burridge (1981). They proposed a hybrid pressure-based coordinate that is particularly popular in hydrostatic NWP models. The respective transformation in z coordinates may be written as

$$z(Z) = Ha(Z) + hb(Z). \quad (7)$$

Here the functionals a and b are usually specified in a table and need to satisfy

$$a(Z = 0) = 0, \quad a(Z = H) = 1,$$
$$b(Z = 0) = 1, \quad b(Z = H) = 0 \quad (8)$$

in order to be consistent with the boundary conditions (3).

In our study we employ an alternative vertical mesh structure where the decay with height of underlying terrain features is stipulated as an exponential function according to

$$z(Z) = Z + h[\alpha e^{-Z/s} + \beta e^{+Z/s}]. \quad (9)$$

The parameters α and β are then specified such as to satisfy the boundary conditions (3); that is,

$$\alpha = \frac{e^{2H/s}}{e^{2H/s} - 1} \quad \beta = \frac{-1}{e^{2H/s} - 1}. \quad (10)$$
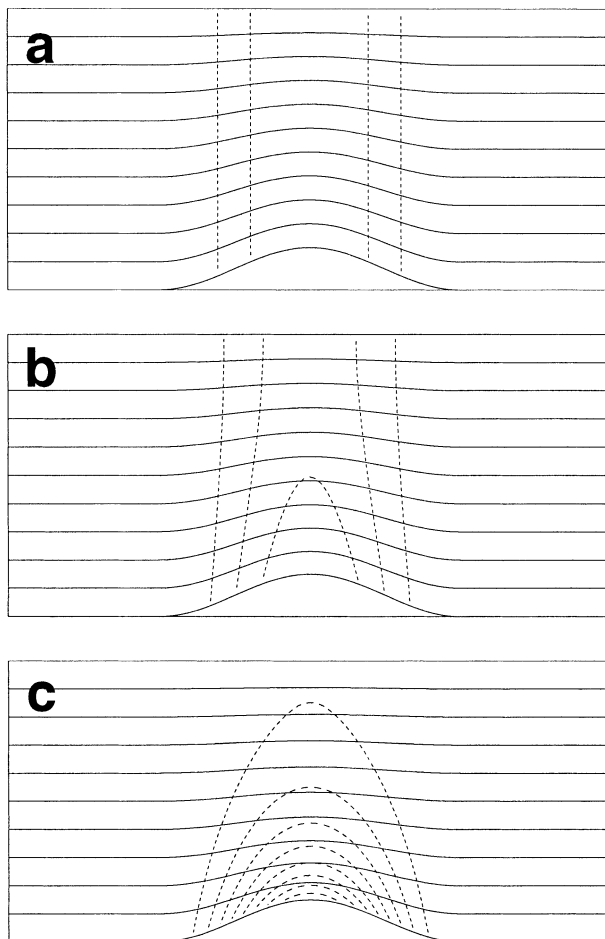
Rearranging the terms simplifies (9) to

FIG. 2. Vertical coordinate (full lines) and inverse of the Jacobian $J^{-1} = \partial z/\partial Z$ (dashed lines, contour interval = 0.05) for three coordinates: (a) sigma coordinate, (b) coordinate with exponential decay (11) based on a value of $s = H$, and (c) as in (b) but with $s = H/3$.

$$z(Z) = Z + h\frac{\sinh[(H - Z)/s]}{\sinh[H/s]}. \quad (11)$$

Here the single scale parameter s plays the role of a scale height; that is, the underlying terrain features approximately decay by a factor $1/e$ over a depth s. With $s \approx H$, the resulting coordinate structure is qualitatively comparable to sigma coordinates. With $s < H$, a hybridlike setting is obtained.

The motivation for using the exponential decay (11) is fourfold: First, unlike with sigma coordinates, the vertical decay affects not only the coordinate height itself, but also the Jacobian and all other metric terms (cf. Figs. 2a and 2b). Second, despite its simplicity, the formulation allows for coordinates that are comparable to classical hybrid formulations (see Fig. 2c). Third, the explicit specification of a decay function by an analytical formula is superior to the specification of the computational levels in a table, since the latter may limit the order of accuracy of the resulting finite-difference approximation. Fourth, the decay function is defined by

one single parameter (the scale height, s), and this simplicity is ideal for sensitivity studies and comparisons as those to be presented in section 3.

While in the following we will restrict our attention to vertical decay functions according to (11), the procedure in the next sections may easily be generalized to coordinates based on any other decay function, as well as to treatments with a stretched spacing of the computational levels.

c. Definition of new coordinate

Currently, most terrain-following coordinates are based on a special class of vertical coordinates that entail a *local* transformation, whereby the transformation at a location (x, y) depends upon the height of the underlying topography alone; that is,

$$Z(x, y, z) = Z(h(x, y), z). \qquad (12)$$

As a result, any terrain feature exhibits the same vertical decay, irrespective of its shape and horizontal scale. The basic concept of the new coordinate is to make better use of the generality of (2), and to employ a *scale-dependent vertical decay* of underlying terrain features. More specifically, the decay rate is selected such that small-scale topographic variations decay much faster with height than their large-scale counterparts. This generalization implies a *nonlocal* transformation not amenable to (12).

In its simplest form, the transformation is defined in terms of two different scale heights, which govern the vertical decay of the larger- and smaller-scale contributions of the topography, respectively. To this end, the topography is split into

$$h(x, y) = h_1(x, y) + h_2(x, y), \qquad (13)$$

where the subscripts 1 and 2 refer to large-scale and small-scale contributions, respectively. In practice, the large-scale contribution h_1 can be obtained from the full topography by an appropriate smoothing operation. The coordinate is then defined by the relationship

$$z(Z) = Z + h_1(x, y)b_1(Z) + h_2(x, y)b_2(Z), \qquad (14)$$

where, following (11), the vertical decay functions are given by

$$b_i(Z) = \frac{\sinh[(H - Z)/s_i]}{\sinh[H/s_i]}. \qquad (15)$$

The second and the third term in (14), respectively, govern the decay with height of large- and small-scale terrain features with the scale heights s_1 and s_2.

All coordinates to be considered in this study may be viewed as special cases of (14). For sigma coordinates (6), the respective functionals read

$$b_1(Z) = b_2(Z) = \frac{H - Z}{H}, \qquad (16)$$

and for the hybrid formulations (11),

$$b_1(Z) = b_2(Z) = \frac{\sinh[(H - Z)/s]}{\sinh[H/s]}. \qquad (17)$$

Similarly both these coordinates may also be interpreted as special cases of the Simmons and Burridge coordinate with $a(Z) = Z/H$.

d. Metric terms

The implementation of a numerical model in the coordinates (x, y, Z) requires the usual transformation of the governing system of equations (e.g., Gal-Chen and Sommerville 1975; Clark 1977). As a result, metric terms appear in the transformed system of equations. In general, the following terms will be needed:

$$J^{-1} = \partial z/\partial Z, \qquad \partial z/\partial X, \qquad \partial z/\partial Y, \qquad (18)$$

where $\partial/\partial X$ and $\partial/\partial Y$ denote derivatives on Z surfaces. In many sigma-coordinate formulations, it is common practice to hard-code the selected transformation. This procedure implies recomputing the metric terms whenever needed. With the new transformation it will be more efficient to store all or some of the metric terms as a function of the three-dimensional grid.

The computation of the metric terms may be performed using the analytical definition of the coordinate based on (14) and (15). In practice, however, it will often be more convenient to compute the metric terms using finite differences. For instance, consider an Arakawa C grid, which uses velocity components $D\mathbf{X}/Dt = (u, v, W)$ that are staggered by half-grid increments in the respective directions. For this grid, $z(x, y, Z)$ can be defined on a staggered mesh as $z_{i,j,k+1/2}$ based on (14) and (15). Finite differences can then be employed to compute $(J^{-1})_{i,j,k}$ at the mass point i, j, k of the grid. This treatment is also consistent with the properties of conservative finite-difference approximations.

e. Invertibility condition and choice of vertical decay rate

According to (4), the invertibility condition implies that $Z(z)$ is a strictly monotone function. With (14) and (15) this yields

$$J^{-1} = \frac{\partial z}{\partial Z} = 1 - \frac{h_1}{s_1} \frac{\cosh[(H - Z)/s_1]}{\sinh[H/s_1]}$$
$$- \frac{h_2}{s_2} \frac{\cosh[(H - Z)/s_2]}{\sinh[H/s_2]} > 0. \qquad (19)$$

This condition is most restrictive on the surface level $Z = 0$ where the hyperbolic cosine terms have maximum amplitude. A sufficient (but not necessary) condition of invertibility can thus be expressed as
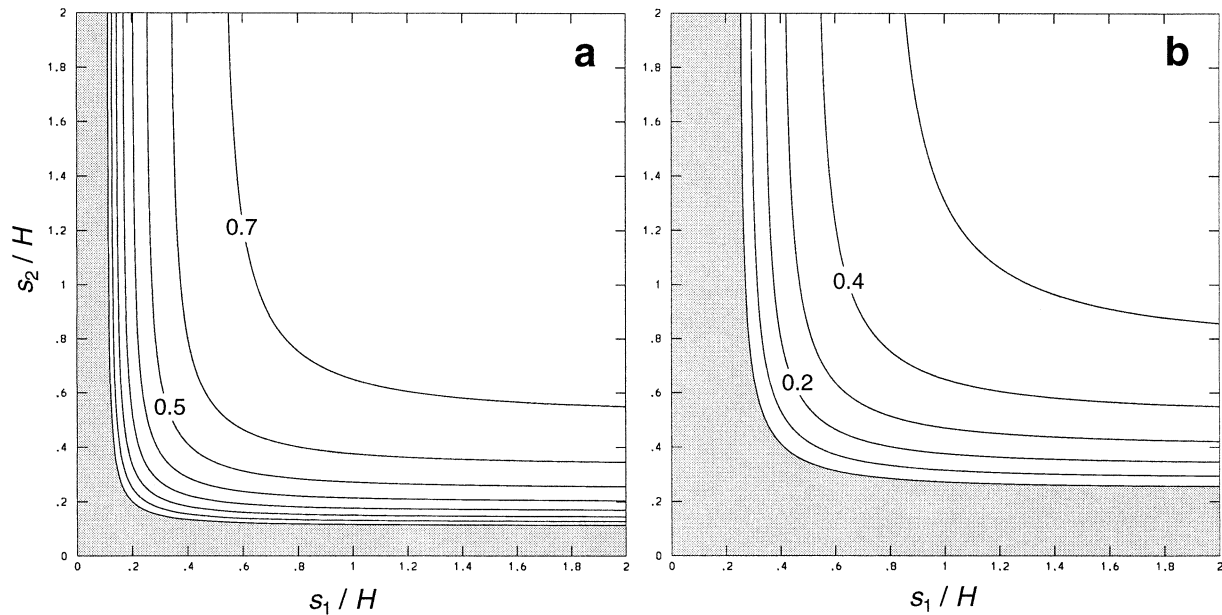
FIG. 3. Dimensionless display of γ according to (20) providing a lower bound to the Jacobian J of the new coordinate transformation. The horizontal and vertical axes are spanned by dimensionless values of the two scale heights for topographic features, respectively: (a) for $h_{1,max}/H = h_{2,max}/H = 0.1$ and (b) for $h_{1,max}/H = h_{2,max}/H = 0.05$. Settings of $(s_1/H, s_2/H)$ in the gray area have $J \leq 0$ and violate the invertibility condition.

$$\gamma := 1 - \frac{h_{1,max}}{H} \frac{H}{s_1} \coth\left(\frac{H}{s_1}\right)$$

$$- \frac{h_{2,max}}{H} \frac{H}{s_2} \coth\left(\frac{H}{s_2}\right) \geq 0, \qquad (20)$$

where $h_{i,max} = \max_{x,y}[h_i(x, y)]$. The term γ always satisfies $\partial z/\partial Z \geq \gamma$ and thus measures how close a coordinate definition based upon values of (s_1, s_2) is located to the invertibility threshold. In addition, γ provides a dimensionless measure of the minimum thickness of the lowermost coordinate layer as well as pertinent information on the vertical advective Courant number:

$$\alpha_z = \frac{w\Delta t}{\Delta z} \leq \frac{1}{\gamma}\frac{w\Delta t}{\Delta Z}. \qquad (21)$$

Explicit formulations with small values of γ may require a reduction of the time step to ensure a stable integration, as the coordinate transformation compresses the computational layers.

Equation (21) is used in Fig. 3 to plot the invertibility condition γ for selected pairs of $(h_{1,max}/H, h_{2,max}/H)$ as a function of $(s_1/H, s_2/H)$. The optimal choice of the scale heights s_i will depend upon the problem under consideration. For many atmospheric applications it appears optimal to choose $s_1 \approx 10$ km and, subsequently, to minimize s_2 for a specified value of $\gamma > 0$. Such a setting will achieve two goals: quasi-horizontal computational surfaces in the stratosphere, and a rapid decay of small-scale terrain features within the troposphere. In general, the invertibility condition (20) appears not

to be seriously limiting. For instance, for a topography characterized by $h_{1,max} \approx h_{2,max} \approx 1500$ m and a model domain with $H = 25$ km, the values $s_1 = 15$ km and $s_2 = 2.5$ km represent a legitimate choice with $\gamma = 0.29$.

It is important to realize that the splitting of the topography into two contributions is the key to attaining a rapid vertical decay of the small-scale topographic features. For instance, the vertical decay of the SLEVE setting with $\gamma = 0.29$ alluded to above cannot be matched by any hybrid formulation. More specifically, using $s = 2.5$ km with the hybrid setting (11) leads to $\gamma = -0.2$, thus representing a noninvertible coordinate setting. The inability of the hybrid formulation to attain a rapid vertical decay is not surprising: With a topographic height of $h = 3$ km, it is definitively not possible to prescribe quasi-horizontal computational levels at a height of 2.5 km. Only the splitting of the topography allows choosing a small s_2 value that is comparable or smaller than the total mountain height. This is indeed why a combination with $s_1 \gg s_2$ is so advantageous.

3. Idealized advection test

a. Overview

To quantify coordinate transformation errors, a simple two-dimensional advection test is used. Its main features are sketched in Fig. 4. To mimic the effects of complex topography, we employ an obstacle with a finescale substructure (the wavelike features). The wavelength of this structure is typically set to eight-gridpoint increments,
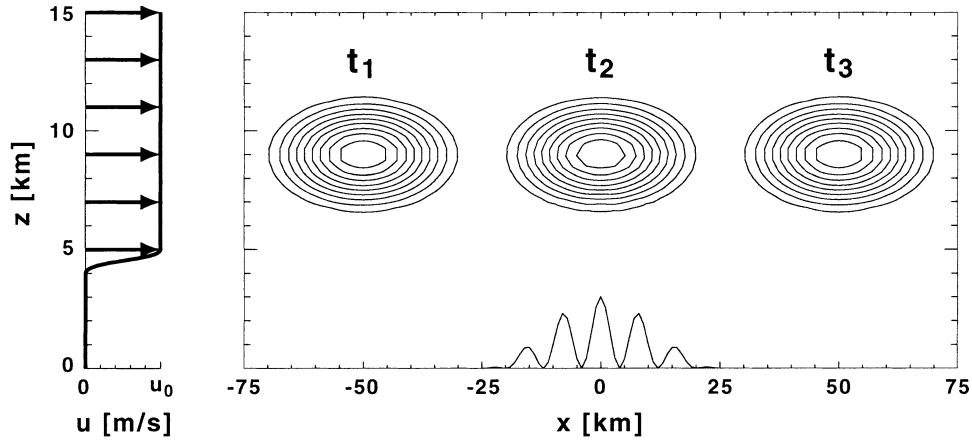
FIG. 4. Vertical cross section of the idealized two-dimensional advection test. The topography is located entirely within a stagnant pool of air, while there is a uniform horizontal velocity aloft. The analytical solution of the advected anomaly is shown at three instances.

that is, to a scale that is usually retained in digital topography fields used in weather prediction and climate models.

The topographic obstacle is submerged within a stagnant air mass, but aloft there is a uniform and purely horizontal flow directed from left to right. This upper-level flow is separated from the stagnant low-level pool by a shear layer. The situation thus corresponds to the not uncommon meteorological condition of a low-level blocked air mass with submerged topography. The upper-level flow represents plain horizontal and linear advection, but in the presence of coordinate deformations as implied by the underlying topography.

To test the performance of various schemes, a simple scalar anomaly is initialized upstream of the topography and advected by the flow. The transport of the anomaly field ρ is described in conservative flux form by

$$\partial\rho/\partial t + \mathbf{\nabla}\cdot(\mathbf{v}\rho) = 0, \qquad (22)$$

where $\mathbf{v} = (u, v, w) = (u(z), 0, 0)$ is the specified velocity vector. On a regular grid, the advection is along the coordinate surfaces. On a terrain-following computational mesh, however, the flow becomes multidimensional. In two dimensions, the transformed equation reads

$$\frac{\partial}{\partial t}(J^{-1}\rho) + \frac{\partial}{\partial X}(J^{-1}u\rho) + \frac{\partial}{\partial Z}(J^{-1}W\rho) = 0, \qquad (23)$$

where $W = DZ/Dt$ is the vertical velocity expressed in the new coordinate framework. The prescribed wind profile $u(z)$ can be expressed as

$$(u, w) = (-\partial\phi/\partial z, 0)$$

using a streamfunction $\phi = \phi(z)$. Transformation into computational space then yields

$$(u, W) = J\left(-\frac{\partial\phi}{\partial Z}, \frac{\partial\phi}{\partial X}\right). \qquad (24)$$

Introducing (24) into (23), one obtains

$$\frac{\partial}{\partial t}(J^{-1}\rho) + \frac{\partial}{\partial X}\left(-\frac{\partial\phi}{\partial Z}\rho\right) + \frac{\partial}{\partial Z}\left(\frac{\partial\phi}{\partial X}\rho\right) = 0. \qquad (25)$$

Choosing (25) rather than (23) as the governing equation for the numerical implementation has two important advantages. First, (25) allows implementing the nondivergence property of the specified flow field on the level of the numerical approximation. Second, in (25) the metric terms disappear in the flux-divergence computation, such that the cancellation problems addressed by KSF are avoided. In general, however, (25) is not amenable, as the streamfunction may not be available, or as the wind field may be divergent.

For all tests we use a computational domain that is confined above by a rigid lid at $H = 25$ km and that is periodic in the x direction. The anomaly is initialized at t_1 and advected from left to right. Diagrams will be shown at three times corresponding to positions of the anomaly upstream, over and downstream of the obstacle (see Fig. 4).

The standard experiments will be conducted using explicit time stepping with centered finite differences in space and time (leapfrog) on a staggered Arakawa C grid. Other schemes to be considered include higher-order versions of the leapfrog scheme, the upstream scheme, and two versions of the Smolarkiewicz scheme (Smolarkiewicz 1984). Unless stated otherwise, the numerical experiments are conducted in the absence of explicit diffusion.

Tests are conducted using the four different coordinates shown in Fig. 5. The first mesh is obtained with a sigma coordinate (Fig. 5a). The second mesh is a hybridlike setting (Fig. 5b), based upon (11) with a scale height of $s = 8$ km. This coordinate is characterized by a more rapid decay of the terrain features with height. The third mesh (Fig. 5c) is a version of the SLEVE coordinate (14). It requires splitting the topography according to (13) into larger-scale and smaller-scale con-
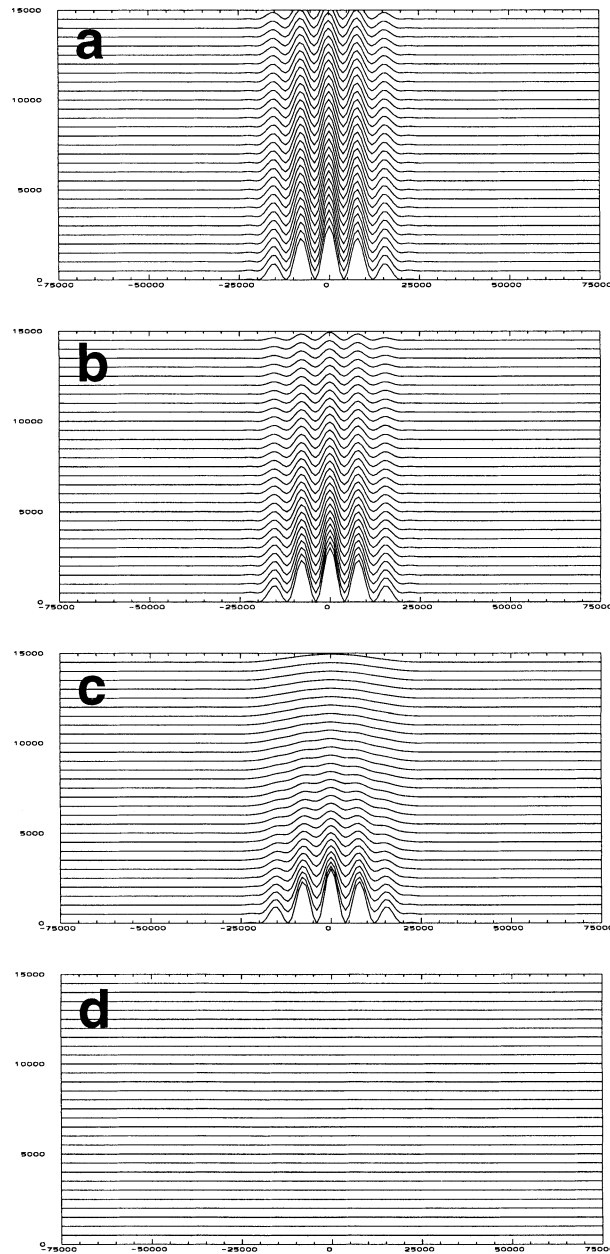
FIG. 5. Vertical coordinates used for the idealized advection test: (a) sigma coordinate, (b) hybrid coordinate with a scale height of $s = 8$ km, (c) SLEVE coordinate using a scale-dependent decay of terrain features ($s_1 = 15$ km for large- and $s_2 = 2.5$ km for small-scale features, respectively), and (d) reference grid without topography. The diagrams show the lowermost 15 km of the computational domain with a depth of $H = 25$ km.

tributions (see details in next subsection). For the two scale heights, we use $s_1 = 15$ km and $s_2 = 2.5$ km. The resulting mesh (Fig. 5c) has a much smoother structure at upper levels. It is comparable to the hybrid coordinate (Fig. 5b) in the sense that the maximum displacement of the coordinate surfaces from their upstream level are almost identical (e.g., the maximum displacement for both these coordinates is ~500 m at a height of 15 km).

As a reference, an integration in the absence of topography is also conducted (Fig. 5d). This integration will allow distinguishing between the regular-grid truncation error of the finite-difference scheme and the errors associated with coordinate transformations.

b. Detailed specification of the advection test

We consider a computational domain with a length of 300 km and a depth of 25 km. The topography $h(x)$ is specified as the product of a large-scale mountain $h*(x)$ of halfwidth a, and a small-scale wavelike perturbation of wavelength λ; that is,

$$h(x) = \cos^2\left(\frac{\pi x}{\lambda}\right) h*(x), \qquad (26a)$$

where

$$h*(x) = \begin{cases} h_o \cos^2\left(\frac{\pi x}{2a}\right) & \text{for } |x| \leq a \\ 0 & \text{for } |x| \geq a \end{cases} \qquad (26b)$$

and where h_o denotes the maximum height of the obstacle. In all examples we use $h_o = 3$ km, $a = 25$ km, and $\lambda = 8$ km. For the formulation with the new coordinate, the topography is split into larger-scale and smaller-scale contributions; see (13). To this end, we choose for the larger-scale contribution

$$h_1(x) = \frac{1}{2} h*(x). \qquad (27)$$

This implies that the two contributions have the same maximum amplitude of 1.5 km.

The discretization uses an Arakawa C grid. All numerical operations are coded in conservative flux form. An Asselin filter was implemented, but is not activated for the tests presented. The height z of the coordinate surfaces is discretized from (14) at the W points of the grid, using the respective definitions for the three coordinate systems considered, that is, (15), (16), and (17). The Jacobian is then defined at the mass points of the grid. The sheared wind profile is specified as

$$u(z) = u_o \begin{cases} 1 & \text{for } z_2 \leq z \\ \sin^2\left(\frac{\pi}{2} \frac{z - z_1}{z_2 - z_1}\right) & \text{for } z_1 \leq z \leq z_2 \\ 0 & \text{for } z \leq z_1 \end{cases} \qquad (28)$$

with $u_o = 10$ m s^{-1}, $z_1 = 4$ km, and $z_2 = 5$ km. The wind field is defined by means of a streamfunction

$$\phi(z) = -\int_0^z u(z)\, dz \qquad (29)$$

and implemented according to (25). We define the streamfunction at doubly staggered locations $\phi_{i+1/2,k+1/2}$, and its derivatives $(\partial\phi/\partial Z)_{i+1/2,k}$ and $(\partial\phi/\partial X)_{i,k+1/2}$ at staggered

locations using centered finite differences of second-order accuracy.

The anomaly is assigned the shape

$$\rho(x, z) = \rho_o \begin{cases} \cos^2\left(\dfrac{\pi r}{2}\right) & \text{for } r \leq 1 \\ 0 & \text{else} \end{cases} \quad \text{with}$$

$$r = \left[\left(\frac{x - x_o}{A_x}\right)^2 + \left(\frac{z - z_o}{A_z}\right)^2\right]^{1/2} \quad (30)$$

and initialized at time $t_1 = 0$ at location $(x_o, z_o) = (-50$ km, 9 km) with amplitude $\rho_o = 1$ and halfwidths $A_x = 25$ km, $A_z = 3$ km. At time $t_2 = 2500$ s, the anomaly is centered right over the mountain and the integrations are terminated at $t_3 = 5000$ s.

Unless stated otherwise, the discretization involves 300×50 grid points with grid increments of $\Delta x = 1$ km and $\Delta Z = 500$ m. The time step is $\Delta t = 25$ s yielding an advective Courant number of $\alpha_x = u\Delta t/\Delta x = 0.25$ in the horizontal direction. The maximum Courant numbers $\alpha_z = |W\Delta t/\Delta Z|$ in the vertical direction amount to 0.47, 0.34, 0.12, and 0 for the four coordinates considered, respectively (cf. Fig. 6).

c. Results for centered differencing

We start by discussing the results using centered finite differences in space and time (leapfrog). The numerical solutions and the error fields for the four coordinates systems of Fig. 5 are displayed in Fig. 6. The top panels of Fig. 6 are for the sigma coordinate. As the anomaly is located over the obstacle, substantial distortions as well as spurious smaller-scale features are evident. The error field valid at t_3 (Fig. 5b) shows a smooth error structure downstream, with a maximum amplitude corresponding to between -17% and $+16\%$. Upstream of the obstacle, the error field has a much finer scale. These characteristics are consistent with the well-known phase errors of centered schemes (e.g., Durran 1998). In particular, the finescale errors upstream of the obstacle result from negative group velocities associated with small-scale waves (numerical dispersion).

Using the hybridlike coordinate in Figs. 6c,d substantially reduces the numerical errors. Maximum errors are now between -6% and $+4\%$. Furthermore, the error notably decreases over the depth of the anomaly as a function of height, in response to the strong vertical gradient in the coordinate deformation.

With the SLEVE coordinate, the error is reduced to $\sim 2\%$ (see Figs. 6e,f). The error field is almost identical to that of the reference solution in the absence of topography (cf. Figs. 6g,h). Thus, for this coordinate the error is dominated by the regular truncation error of the scheme, while for the sigma and hybrid coordinate it is dominated by transformation errors associated with the heavily distorted grid. A summary of the error measures can be found in Table 1.

The large errors resulting from the sigma and hybrid coordinates are not surprising. For illustration, Fig. 7 displays the analytical solution in computational space (full lines), along with contours of constant z height (dashed lines). This display serves to illustrate the strong distortions that occur in computational space. The magnitude of the errors in the different panels of Fig. 6 seems approximately proportional to the distortion of the computational grid.

d. Results for fourth-order centered schemes

Next consideration is given to centered differences of fourth-order accuracy using the sigma coordinate (as in Figs. 6a,b). The results (Fig. 8) show that increasing the order of accuracy has a very pronounced and highly beneficial impact upon the quality of the solutions. The positive impact of fourth-order horizontal advection is of practical interest, noting that many of today's numerical weather prediction models are accurate to only second order. Figure 8 suggests that a careful reconsideration of such choices might be appropriate, taking into account the presence of terrain-following grids. Apparently, the beneficial aspects of higher-order horizontal advection are not merely restricted to reducing the amplitude and phase errors associated with small-scale anomalies, but also make the horizontal advection of large-scale anomalies less sensitive to the presence of small-scale features in the computational grid. In this context it is worth noting that most of the positive impact seen in Fig. 8 is due to the use of fourth-order accuracy in the horizontal direction, while the use of fourth-order accuracy in the vertical has little additional impact. This suggests that the poor behavior seen in Figs. 6a,b is primarily due to the lack of horizontal (rather than vertical) resolution/accuracy, a result that will be confirmed in section 3f below.

e. Results for forward-in-time schemes

The results for the first-order upstream scheme using forward time stepping are shown in Fig. 9. This scheme is much more diffusive than the leapfrog scheme considered above. Even the reference solution in the absence of coordinate transformations (Figs. 9g,h) is characterized by an amplitude reduction of 22%. The coordinate transformations in the upper panels of Fig. 9 have a devastating effect upon the performance of the scheme. With the sigma coordinate, the amplitude of the anomaly is reduced by almost 72%!

Additional tests were performed for two versions of the second-order multidimensional positive definite advection transport algorithm (MPDATA) scheme (Smolarkiewicz 1984). This scheme is popular due to its small phase errors and positive-definite treatment, and is particularly well suited for the advection of chemical con-
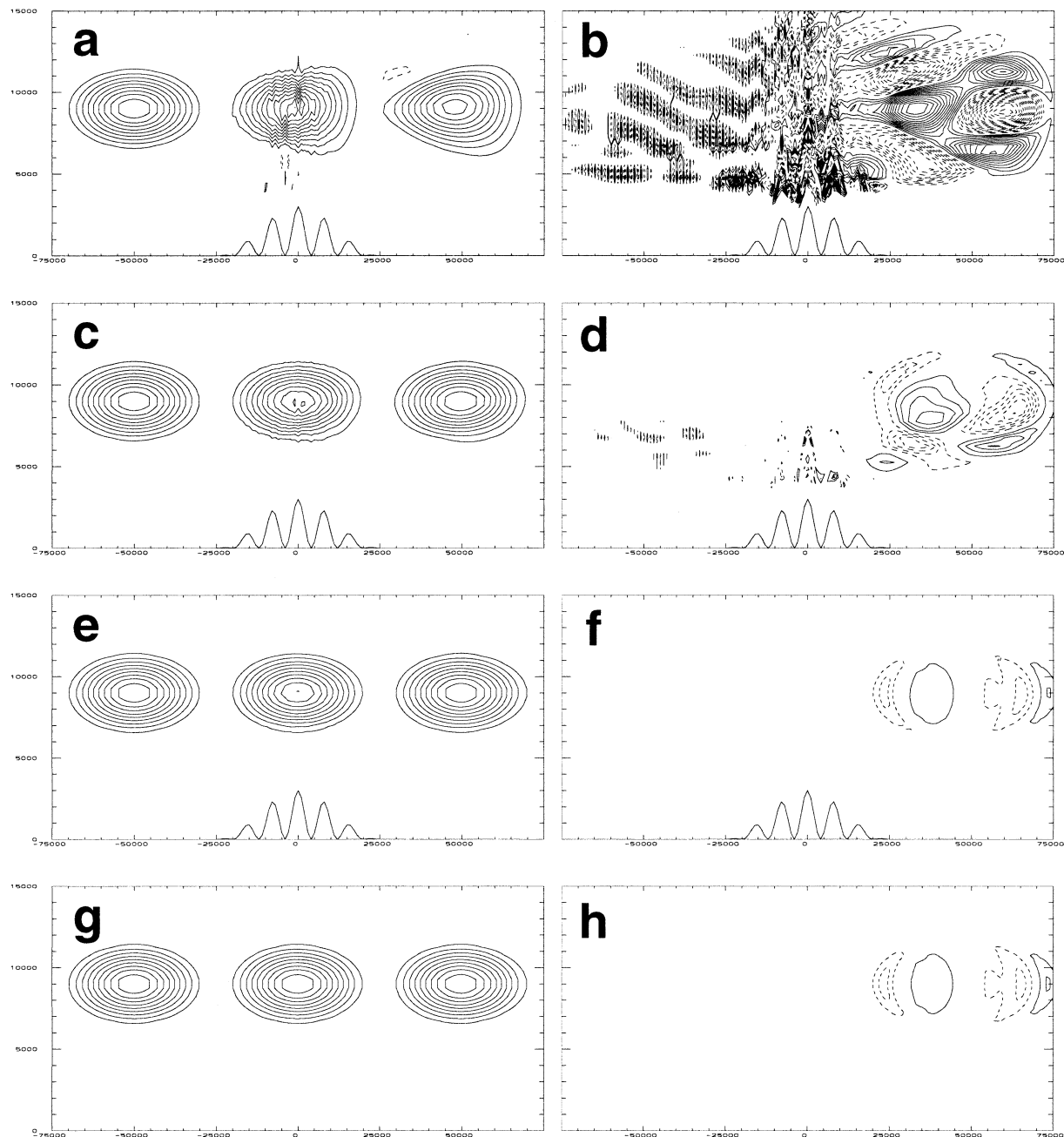
FIG. 6. Numerical solutions to the advection test using centered differences and a horizontal Courant number of $\alpha = 0.25$. (a),(c),(e),(g) The advected anomalies at three consecutive times ($t_1 = 0$, $t_2 = 2500$ s, $t_3 = 5000$ s) and (b),(d),(f),(h) the error field at t_3 (numerical minus analytical field). The solutions are from numerical experiments using (a),(b) the sigma coordinate, (c),(d) a hybrid coordinate, (e),(f) the SLEVE coordinate, and (g),(h) a regular grid. The initial amplitude of the anomaly is 1; the contour interval in the left-hand panels is 0.1, and that in the right-hand panels is 0.01 (zero contour suppressed, negative contours dashed). The coordinate systems are shown in Fig. 5.

stituents and water species. We consider both the nonlinear version of the scheme as described in Smolarkiewicz (1984), and a version using a linearized antidiffusive correction. Results are summarized in Table 1. Despite the excellent performance of the scheme in the absence of grid transformations, the deteriorating effects of coordinate transformations are evident.

The results of these tests can be summarized as follows: Schemes with implicit diffusion suffer particularly large coordinate transformation errors. Diffusion spreads out the solution in computational space, rapidly broadens the initial anomaly, and thereby makes the scheme more susceptible to coordinate transformations.

TABLE 1. Error measures of numerical solutions to the standard version of the advection test for five numerical schemes and four vertical coordinate formulations. The upper line for each coordinate entry lists the extremes of the numerical solution (analytical values are 0 and 1), the lower line shows the maximum errors with respect to the analytical reference solution.

		Leapfrog		Leapfrog, fourth order		Upstream		MPDATA		MPDATA linearized	
		min	max	min	max	min	max	min	max	min	max
Sigma	ρ	−0.168	0.953	−0.058	1.001	0.000	0.284	0.000	0.605	−0.076	0.736
	$\rho_{num} - \rho_{ana}$	−0.174	0.162	−0.057	0.052	−0.700	0.213	−0.396	0.206	−0.269	0.179
Hybrid	ρ	−0.050	0.989	−0.023	0.982	0.000	0.408	0.000	0.836	−0.014	0.928
	$\rho_{num} - \rho_{ana}$	−0.058	0.044	−0.023	0.019	−0.586	0.185	−0.187	0.133	−0.085	0.084
SLEVE	ρ	−0.023	0.985	−0.002	0.984	0.000	0.619	0.000	0.960	−0.012	0.981
	$\rho_{num} - \rho_{ana}$	−0.024	0.021	−0.002	0.002	−0.376	0.106	−0.065	0.061	−0.012	0.013
No topography	ρ	−0.023	0.985	−0.002	0.984	0.000	0.762	0.000	0.979	−0.012	0.982
	$\rho_{num} - \rho_{ana}$	−0.023	0.021	−0.002	0.002	−0.220	0.141	−0.025	0.034	−0.012	0.011

f. Sensitivity to horizontal and vertical resolution

Here we investigate how the solution using centered differencing depends upon horizontal and vertical resolutions. When changing the vertical resolution, the same time step (and thus different vertical Courant numbers) as in the standard case is used. When increasing the horizontal resolution, the time step Δt is reduced such as to maintain the horizontal Courant number at a value of 0.25. When decreasing the horizontal resolution beyond that of the standard setting, we maintain the time step, in order to retain the vertical Courant number.

Figure 10 shows the results for the standard test with sigma coordinates (cf. Figs. 6a,b), using four different horizontal resolutions. It can be observed that the transformation errors are highly sensitive. In Fig. 6, we used a horizontal resolution of $\Delta x = 1000$ m, such that the small-scale topographic wavelength corresponds to $\lambda = 8\Delta x$ (for reference, these result are repeated in Figs. 10c,d with a different contour interval). Doubling the resolution to $\Delta x = 500$ m ($\lambda = 16\Delta x$; see Figs. 10g,h) is sufficient to reduce the maximum error from 21% to 3.6%. On the other hand, reducing the resolution to $\Delta x = 1500$ m ($\lambda = 5.3\Delta x$; see Figs. 10a,b) leads to devastating errors with a maximum amplitude of 78%. This result is alarming, as many numerical weather prediction models include appreciable topographic amplitudes in the respective spectral wavelength ranges.

Figure 11 shows the results with three different vertical resolutions. Increasing the number of grid points in the vertical does not improve the behavior of the scheme. Indeed, the error field with increased vertical resolution ($\Delta z = 250$ m; see Figs. 11e,f) is almost identical to the standard experiment ($\Delta z = 500$; see Figs. 11c,d). This is further supported by an additional experiment with lower vertical resolution ($\Delta z = 1000$ m; see Figs. 11a,b), which produces an error field with a slightly reduced amplitude (albeit the anomaly is only poorly resolved at this resolution). This result appears consistent with the experience of operational weather services, who often use their mesoscale NWP models at rather low vertical resolution, and apparently find it more beneficial to invest available computing resources in refining the numerical mesh in the horizontal rather than in the vertical direction.

A more comprehensive analysis of the resolution dependency of the numerical error and its sensitivity with respect to the coordinate formulation under consideration is presented in Fig. 12. The error is defined here as

$$E = \max_{x,z} |\rho_{num} - \rho_{ana}|, \qquad (31)$$

where ρ_{num} and ρ_{ana} denote numerical and analytical solutions at time t_3, respectively. The results for three schemes are summarized in Fig. 12 as a function of horizontal resolution (displayed in dimensionless form as $\lambda/\Delta x$). We first discuss the results for the sigma-coordinate simulations (full symbols). For all schemes considered, convergence is evident in good agreement with the theoretical expectations according to the scheme's order of accuracy (given by the slope of the dashed lines). For short wavelengths around $5\Delta x$, the errors have a magnitude comparable to that of the anomaly. The three schemes differ substantially in their behavior. Taking an error level of $E = 0.1$ as a threshold, it is exceeded for wavelengths smaller than $\sim 13\Delta x$ (MPDATA), $\sim 10\Delta x$ (second-order centered), and $\sim 7\Delta x$ (fourth-order centered), respectively. The simulations using the SLEVE coordinate (open symbols) show a reduction of the error level by a factor ~ 10. For all schemes, this reduction applies to a surprisingly wide range of scales, and there is a striking difference even at wavelengths around $20\Delta x$. As the error induced by the grid transformation heavily depends upon horizontal resolution (see section 4), the SLEVE error curve does not exhibit a regular convergence according to the accuracy of the scheme, but rather the error level approaches that of the sigma coordinate for well-resolved terrain features.

In summary, these results show that the transformation error using the sigma coordinate is most pronounced at horizontal wavelengths around 5 and $10\Delta x$, but its relative magnitude is still substantial at $20\Delta x$. The insensitivity of the results with respect to vertical resolution demonstrates that the main reason for the
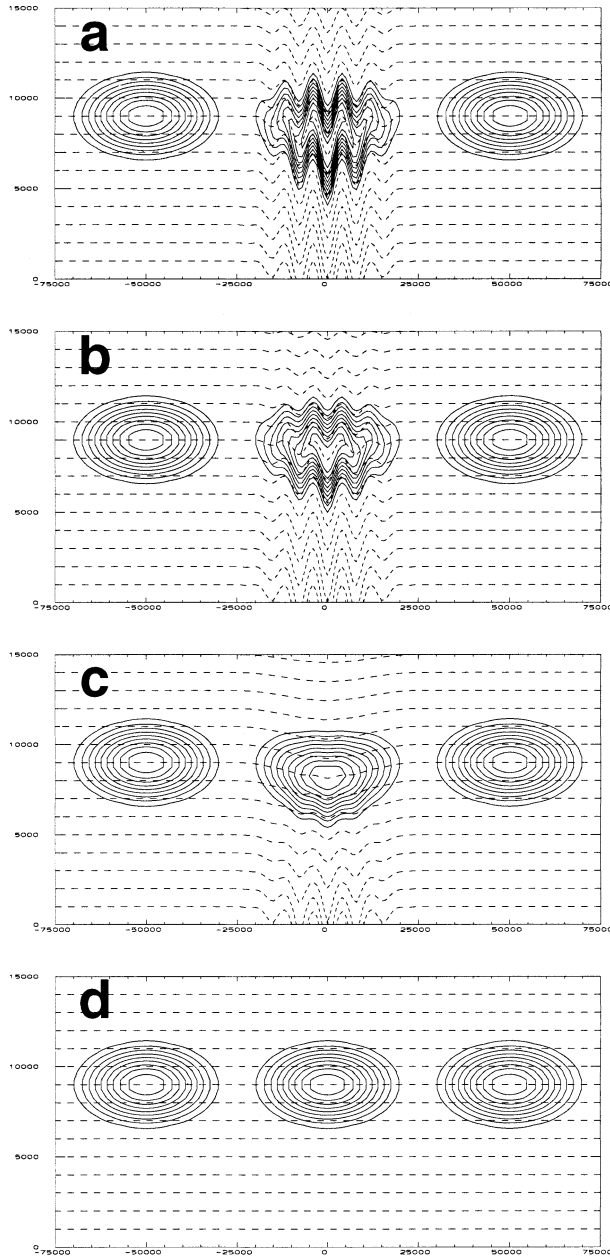
FIG. 7. As in Fig. 6 but showing the structure of the analytical solution at times t_1, t_2, and t_3 (full lines), along with the surfaces of constant height z (dashed lines) in computational (x, Z) space.

error is due to rapid changes of the grid structure in the direction of the flow.

4. Theoretical analysis of truncation error

In this section we carry out a theoretical analysis of the truncation error of the advection equation in the presence of arbitrary coordinate transformations. To simplify the situation, consideration is restricted to the one-dimensional advection equation in conservative flux form:

$$\frac{\partial \rho}{\partial t} + \frac{\partial(u\rho)}{\partial x} = 0, \tag{32}$$

with an arbitrary flow field $u = u(x) > 0$. The performance of the first-order upstream and the second-order centered schemes will be investigated in the presence of an arbitrary coordinate transformation $X = X(x)$. The transformed equation can be written in two ways, either as

$$\frac{\partial \rho}{\partial t} + J\frac{\partial(u\rho)}{\partial X} = 0, \tag{33}$$

or more generally as

$$\frac{\partial \rho}{\partial t} + J\frac{\partial(J^{-1}U\rho)}{\partial X} = 0, \tag{34}$$

where $J = \partial X/\partial x$ is the Jacobian of the transformation and where $U = DX/Dt = Ju$ is the transformed velocity. Multidimensional numerical implementations usually utilize (34). However, for the sake of simplicity and in order to avoid complicating effects associated with the definition of the metric terms (cf. KSF), the subsequent analysis is based on (33).

Since we are interested in the spatial truncation error, (33) will be brought into the form

$$\frac{\partial \rho}{\partial t} + FD = E, \tag{35}$$

where FD is a finite difference approximation of the respective term and E the spatial truncation error. The error term will be derived in the usual way using Taylor series expansions. We will then attempt to split the error term into

$$E = E_{\text{reg}} + E_{\text{trans}}, \tag{36}$$

where the two terms refer to the truncation error associated with finite differencing on a regular grid and the contribution arising from the coordinate transformation, respectively.

a. Upstream differencing

In the case of the upstream scheme on a staggered Arakawa C grid, the approximation reads as

$$FD_i = \frac{J_i}{\Delta X}(F_{i+1/2} - F_{i-1/2}), \tag{37a}$$

with the upstream fluxes given by

$$F_{i+1/2} = u_{i+1/2}\rho_i. \tag{37b}$$

The application of Taylor series expansions delivers the error term:

$$E_u = \frac{\Delta X}{2}J\frac{\partial}{\partial X}\left(u\frac{\partial \rho}{\partial X}\right) + O(\Delta X^2). \tag{38}$$

This equation is formulated in computational space. The transformation back to physical space using $\partial/\partial X = J^{-1}\partial/\partial x$ and $\Delta X = J\Delta x$ is straightforward and yields
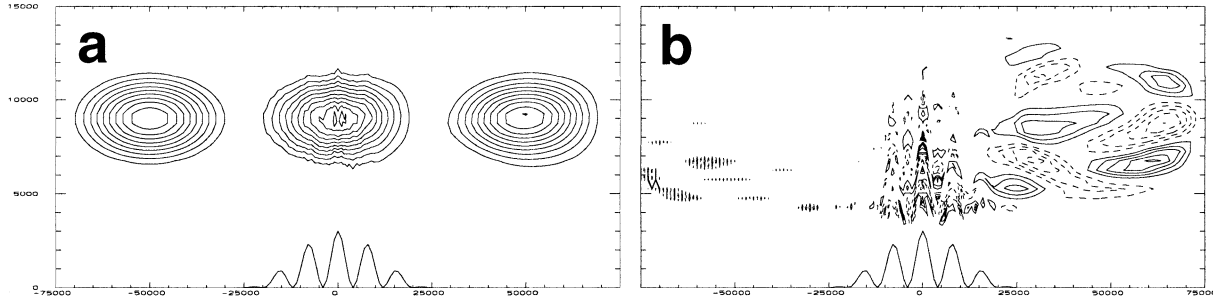
FIG. 8. As in Figs. 6a,b but using fourth-order centered differences.

$$E_u = \frac{\Delta x}{2} J \frac{\partial}{\partial x}\left(u J^{-1} \frac{\partial \rho}{\partial x} \right) + O(\Delta x^2). \qquad (39)$$

In this form, the error term can readily be interpreted. Its amplitude is determined by variations of $u J^{-1}(\partial \rho / \partial x)$, and this implies that variations of the Jacobian J^{-1} play a similar role as those of u or $\partial \rho / \partial x$. The leading error term (39) is now split following (36) into

$$E_{u,\mathrm{reg}} = \frac{\Delta x}{2} \frac{\partial}{\partial x}\left(u \frac{\partial \rho}{\partial x} \right) + O(\Delta x^2), \quad \text{and} \qquad (40a)$$

$$E_{u,\mathrm{trans}} = -\frac{\Delta x}{2} u \frac{\partial \rho}{\partial x} J^{-1} \frac{\partial J}{\partial x} + O(\Delta x^2). \qquad (40b)$$

Equation (40a) represents the standard error contribution associated with upstream differencing on a regular grid, but here $\Delta x = J^{-1}\Delta X$ represents the local value of the grid spacing. Under conditions of uniform flow it simplifies to the error term of linear upstream differencing (see e.g., Durran 1998, p. 39). Equation (40b) represents the contribution associated with grid transformations. It will further be discussed in section 4c below.

b. Centered differencing

In the case of second-order centered differences, (37a) is used with

$$F_{i+1/2} = u_{i+1/2}\frac{1}{2}(\rho_i + \rho_{i+1}). \qquad (41)$$

The application of Taylor series expansions delivers, after some tedious calculations, the error term:

$$E_c = J\frac{\Delta X^2}{24}\left[3\frac{\partial}{\partial X}\left(u \frac{\partial^2 \rho}{\partial X^2} \right) + \frac{\partial^3(u\rho)}{\partial X^3} \right] + O(\Delta X^3). \qquad (42)$$

Transformation back to physical space is quite cumbersome. We thus restrict attention to the case $\partial u/\partial x = 0$, whereupon

$$E_c = J\frac{\Delta X^2}{6} u \frac{\partial^3 \rho}{\partial X^3} + O(\Delta X^3). \qquad (43)$$

Transformation back to physical space delivers

$$E_c = \frac{\Delta x^2}{6} u J^3\left(J^{-1}\frac{\partial}{\partial x} \right)^3 \rho + O(\Delta x^3). \qquad (44)$$

The error may be split according to (36) into

$$E_{c,\mathrm{reg}} = \frac{\Delta x^2}{6} u \frac{\partial^3 \rho}{\partial x^3} + O(\Delta x^3), \quad \text{and} \qquad (45a)$$

$$E_{c,\mathrm{trans}} = J^2\frac{\Delta x^2}{12} u\left[\frac{\partial^2 J^{-2}}{\partial x^2}\frac{\partial \rho}{\partial x} + 3\frac{\partial J^{-2}}{\partial x}\frac{\partial^2 \rho}{\partial x^2} \right] + O(\Delta x^3).$$

$$(45b)$$

In the absence of grid transformations ($J \equiv 1$), the error term again reduces to its classical form.

c. Discussion

Most of the literature on truncation errors of finite-difference approximations restricts attention to simplified cases of uniform flow in the absence of coordinate transformations. Such results may be misleading, as this procedure ignores the error contributions due to deformations of the computational mesh. Indeed, the most important aspect of the above results is that the transformation error E_{trans} has the same leading order as the regular truncation error E_{reg} valid in the presence of a uniform grid. Whether the E_{trans} contribution is relevant depends upon the scales of the flow anomalies and those of the coordinate transformation. Qualitative interpretation of (40) and (45) suggests that the regular-grid contribution to the truncation error will dominate for small-scale flow anomalies, as the coefficient of the leading error term is directly determined by variations of the transported field. However, for larger-scale flow anomalies, the total truncation error will be dominated by transformation errors, as its leading error term has a coefficient that is proportional to horizontal derivatives of the Jacobian. This implies that small-scale grid deformations may be effective in disturbing the transport of large-scale anomalies. This interpretation is consistent with the results of the idealized advection test in section 3.
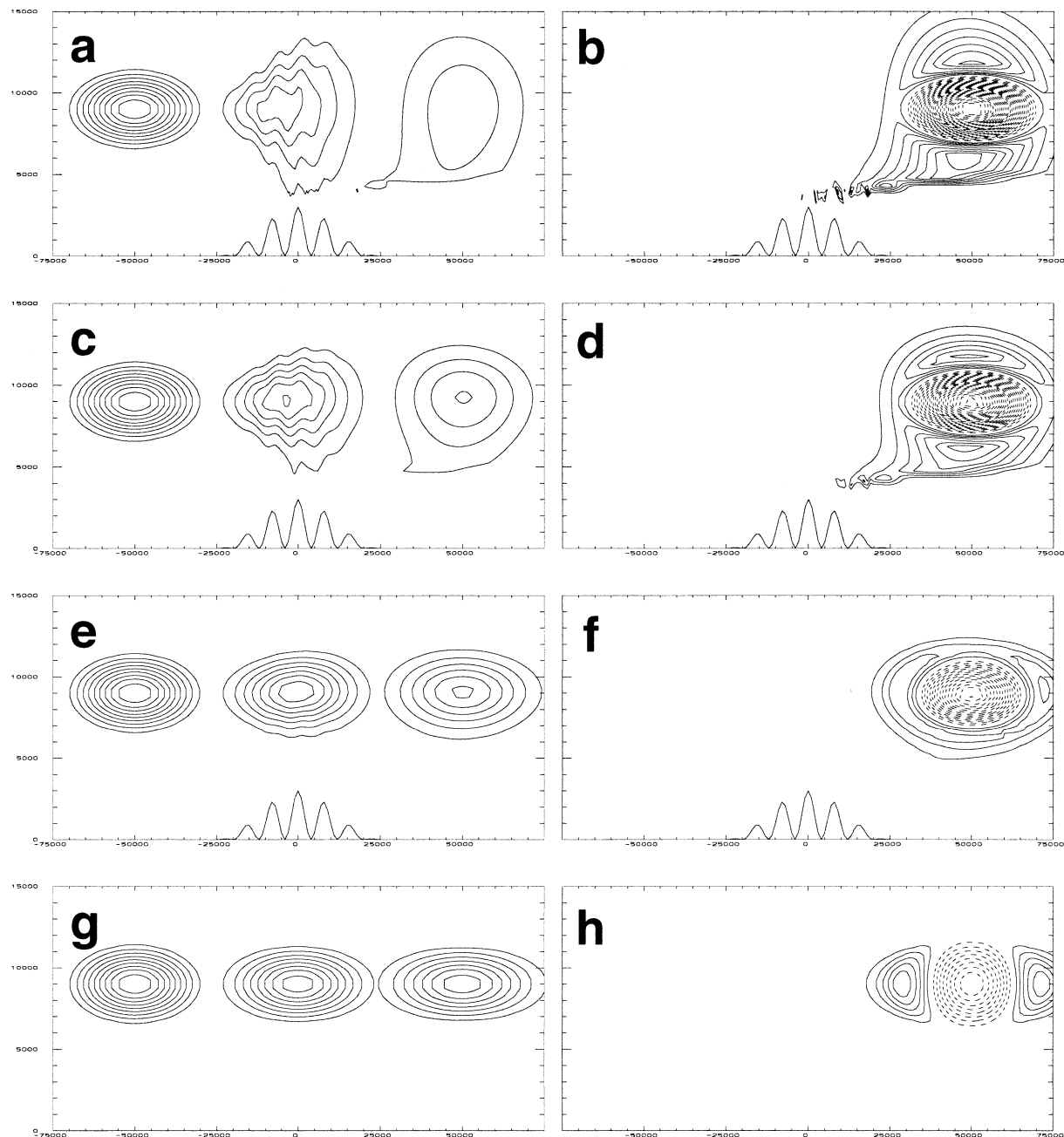
FIG. 9. As in Fig. 6 but for the first-order upstream scheme. Contour interval in the right-hand panels is 0.025.

5. Examples using a fully nonhydrostatic forecasting model

In order to assess the impact of the new coordinate formulation in a NWP context, both idealized and real-case numerical experiments are conducted using the Canadian Mesoscale Compressible Community (MC2) model. This model is based on the nonhydrostatic compressible set of equations and is thus suited for the simulation of atmospheric flows on a wide range of scales.

The prognostic equations for momentum, pressure perturbation, temperature, and specific humidity are discretized on a staggered Arakawa C grid using a semi-implicit, semi-Lagrangian scheme (Tanguay et al. 1990; Benoit et al. 1997). For the solution of the semi-implicit time step, a hydrostatically balanced isothermal reference state is introduced. The model has recently been supplemented with a new adiabatic kernel (Thomas et al. 1998). As a result of using very fast numerical techniques, the MC2 is one of the few models that allows
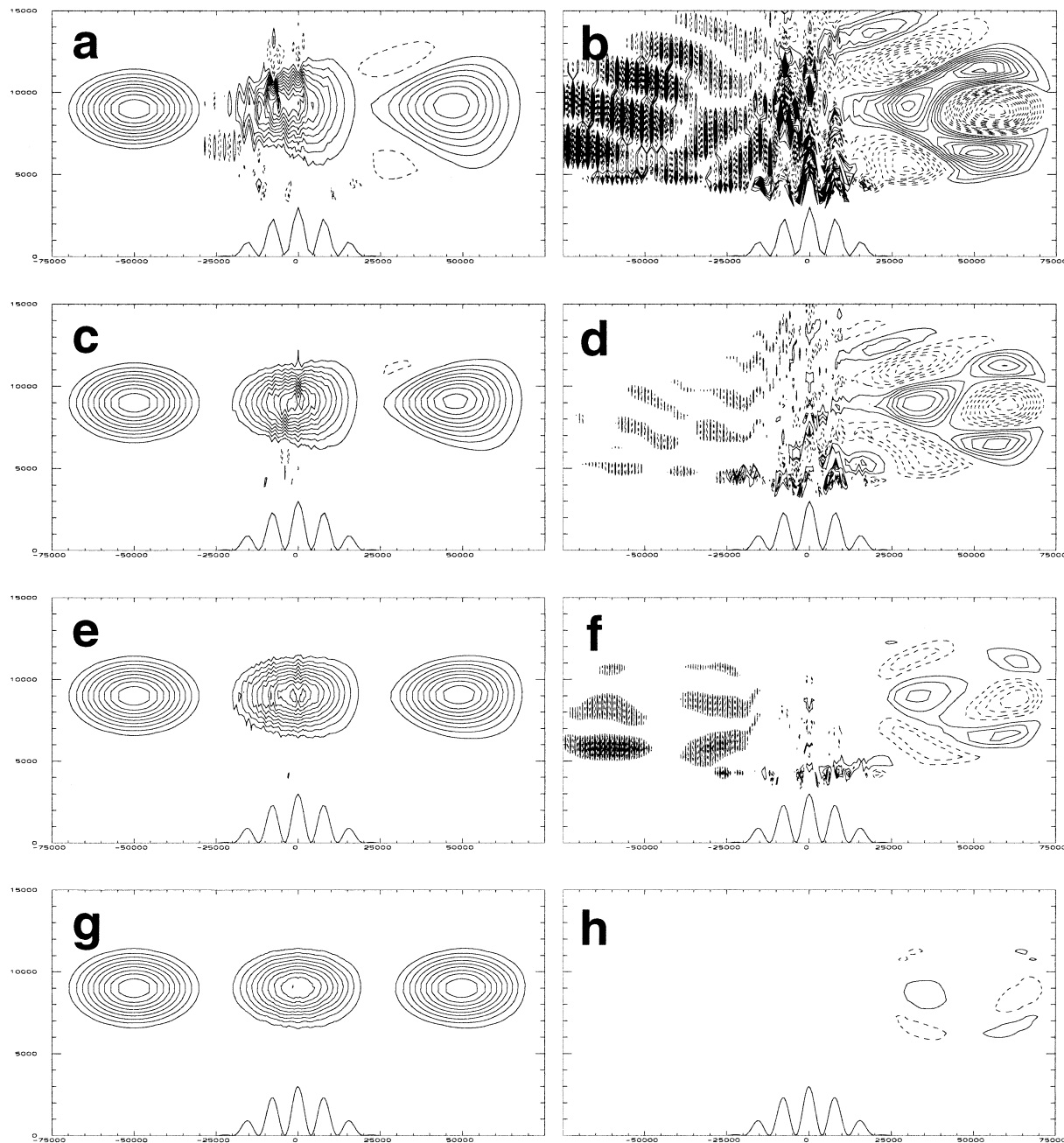
FIG. 10. Solutions using the sigma coordinate with various horizontal resolutions: (a),(b) $\Delta x = 1500$ m, (c),(d) $\Delta x = 1000$ m as in Figs. 6a,b, (e),(f) $\Delta x = 750$ m, and (g),(h) $\Delta x = 500$ m. Conventions are the same as in Fig. 6 except for using a contour interval of 0.02 in the right-hand panels.

conducting high-resolution simulations at convection-resolving resolution in real time on currently available computers. The MC2 is equipped with a sophisticated parameterization package and has extensively been tested for quantitative precipitation forecasting purposes, including the simulation of heavy events (see Benoit et al. 2000, 2002).

a. Implementation of the new coordinate

The original version of the MC2 code uses the sigma coordinate (6), and the metric terms (18) are hard-coded. In order to generalize the formulation for arbitrary coordinate transformations, the code was revised such that the metric terms are stored as a function of the three-dimensional grid. To this end, the height z of the com-
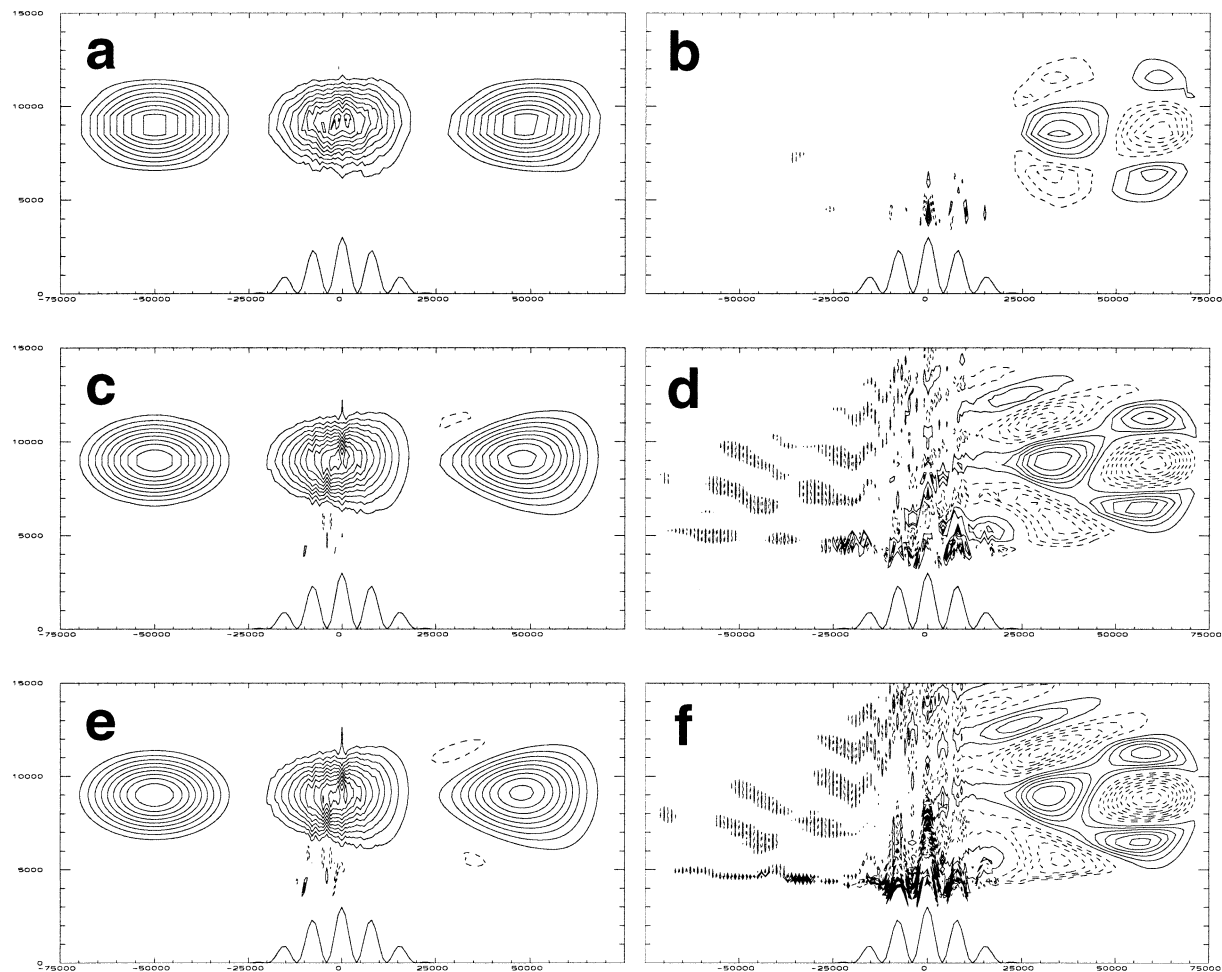
FIG. 11. Solutions using the sigma coordinate with various vertical resolutions: (a),(b) $\Delta Z = 1000$ m, (c),(d) $\Delta Z = 500$ m as in Figs. 6a,b, and (e),(f) $\Delta Z = 250$ m. Conventions are as in Fig. 6 except for using a contour interval of 0.02 in the right-hand panels.
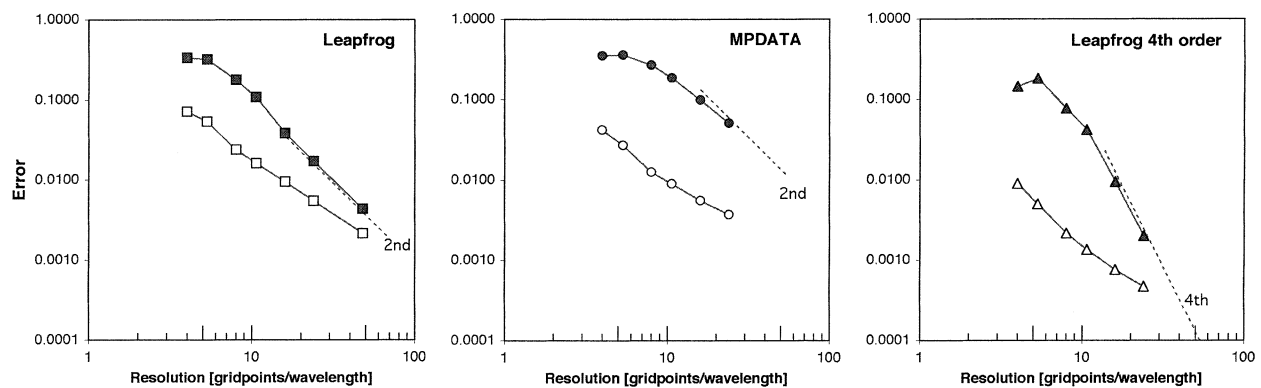

FIG. 12. Errors of the idealized advection test as a function of horizontal resolution for simulations using sigma (filled symbols) and SLEVE coordinates (open symbols). The results pertain to time $t = t_3$ of the test (see Fig. 4). The horizontal resolution is given in dimensionless units of $\lambda/\Delta x$. Results are shown for the second-order and fourth-order leapfrog schemes and the linearized version of the second-order MPDATA scheme. The dashed lines depict the slopes according to second- and fourth-order convergence rates, respectively.

putational levels is computed using (14) and discretized as described in section 3d. All metric terms are then computed from this field using centered finite differences on the staggered grid. The impacts of these changes in terms of execution time and memory requirements are small.

Implementation of the new coordinate (14) requires the splitting of the terrain h into its scale-dependent contributions h_1 and h_2 following (13). To this end, the large-scale contribution h_1 is computed from h by multiple applications of a simple second-order Laplace filter. In our case the filter was applied 100 times, which is sufficient to remove 98% or more of the small-scale variations with wavelengths smaller than $15\Delta x$. In order to remove the small-scale variations along the boundaries, we have extended h by one grid point in each direction, such that for each application of the filter the values outside the boundary are taken from inside the boundary (in one dimension; this is, $h_{i=0} := h_{i=2}$, etc.). This ensures that h_1 becomes smooth over the whole computational domain. The small-scale contribution h_2 is finally obtained as $h_2 = h - h_1$.

b. Dry flow past idealized topography

Here we present results from an idealized experiment of stably stratified, dry flow impinging upon a two-dimensional mountain ridge. The upstream profile is defined by constant values of the Brunt–Väisälä frequency N and the velocity U in the x direction, together with the upstream surface temperature T_o and pressure p_o. The mountain ridge is assigned a bell-shaped structure with superposed small-scale variations:

$$h(x) = h_o \exp\left[-\left(\frac{x}{a}\right)^2\right] \cos^2\left(\frac{\pi x}{\lambda}\right), \qquad (46)$$

where $h_o = 250$ m, $a = 5$ km, and $\lambda = 4$ km. The gravity waves forced by this terrain have two dominating spectral components: a larger-scale hydrostatic wave that is characterized by deep vertical propagation, and smaller-scale waves generated by the cosine-shaped terrain variations and characterized by rapid decay with height due to nonhydrostatic effects.

Assuming a fixed ratio a/λ, the adiabatic and inviscid response in the absence of background rotation is governed by two dimensionless parameters. These are the dimensionless mountain height Nh_o/U and the dimensionless mountain width Na/U. Thus, settings with a constant ratio N/U are dynamically similar, that is, differ only by some scaling.

Simulations are conducted in a model domain with an extent of $L = 200$ km times $H = 19.5$ km. The vertical discretization of the domain is performed on 65 equally spaced layers. A Rayleigh-damping layer with a depth of 30 layers is used to minimize the reflection of vertically propagating waves at the upper boundary. The integrations are carried out until a quasi-steady state

TABLE 2. Settings for the simulations in Fig. 13.

	Figs. 13a,c,e	Figs. 13b,d,f
N (s^{-1})	0.01	0.018 71
U (m s^{-1})	10	18.71
Δx (m)	500	1000
Δt (s)	8	5.34
T_o (K)	288	273.16
p_o (hPa)	1000	1000

is reached and are performed in the absence of any physical parameterization and explicit diffusion. Only the central portion of the domain will be displayed.

In order to explore the sensitivity of the response with respect to the numerical resolution and the choice of the vertical coordinate, a comprehensive set of numerical simulations has been conducted for $N/U = 10^{-3}$ m^{-1}. To provide an overview of the wide range of results, two settings are discussed in more details. These employ values of $N = 0.01$ s^{-1} and $N = 0.01871$ s^{-1} (see Table 2 for additional settings) and are shown in the left- and right-hand panels of Fig. 13, respectively. Both simulations use a hydrostatically balanced isothermal reference state. This is relevant to the comparison, as the upstream profile of the second (but not the first) setting coincides with the reference state.

For both settings, the sigma coordinate given by (6) is compared against a hybridlike coordinate (9) with a scale height of $s = 3$ km ($\gamma = 0.92$), and the SLEVE coordinate (14) with $s_1 = 5$ km and $s_2 = 2$ km ($\gamma = 0.90$). A linear solution based on Fourier decomposition serves as a reference (see Lüthi et al. 1989) and is shown in Fig. 13g.

The simulation with $N = 0.01$ s^{-1} (left-hand panels of Fig. 13) uses a comparatively fine horizontal resolution, such that the small-scale wavelike perturbation of the mountain is associated with a wavelength of $\lambda = 8\Delta x$. The results using the sigma coordinate (Fig. 13a) show a dramatically distorted unphysical wave pattern at upper levels. The error is evident from comparison against the linear solution (Fig. 13g). The solutions using the hybridlike coordinate (Fig. 13c) and the new coordinate (Fig. 13e) show a considerable reduction of these errors. In particular, consistent with theoretical considerations and the linear solution, only the larger-scale mountain waves propagate, while the smaller-scale waves rapidly decay with height.

The simulation in the right-hand panels of Fig. 13 uses a coarser horizontal resolution ($\lambda = 4\Delta x$) and a stratification that matches that of the isothermal reference state of the numerical formulation. Despite the coarser resolution, the standard simulation using sigma coordinates (Fig. 13b) is very successful in comparison to Fig. 13a. The improvements from the hybrid and SLEVE coordinates are quite visible but comparatively small (Figs. 13d,f).

Further analysis demonstrates that the finescale errors seen in Figs. 13a,c are primarily due to the differing
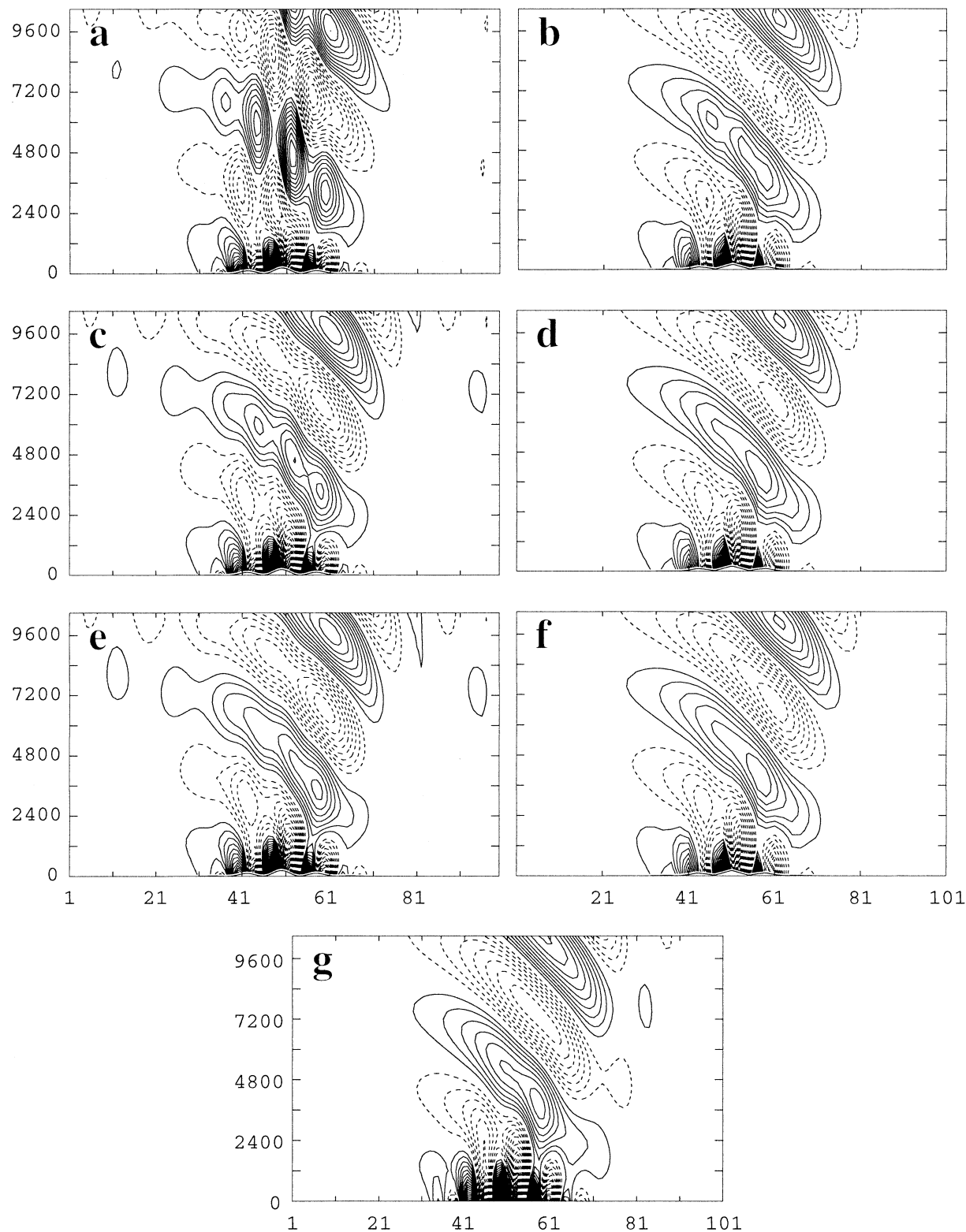
FIG. 13. Simulations of idealized flow past topography based on dynamically equivalent settings with (a),(c),(e) $N = 0.01$ s^{-1} and (b),(d),(f) $N = 0.01871$ s^{-1} (see Table 2 and text for details). Shown are contours of steady-state vertical velocity for numerical solutions using the (a),(b) sigma coordinates, (c),(d) hybrid coordinates, (e),(f) SLEVE coordinates, and (g) for an analytical solution. The contour intervals in the left- and right-hand panels are 0.05 and 0.09355 m s^{-1}, respectively.

stratification of the upstream profile on the one hand, and the reference state used for the semi-implicit time step on the other hand. This is consistent with Pinty et al. (1995), who have detected the importance of the reference state for simulations of gravity wave propagation. However, Pinty et al. restrict attention to comparatively well-resolved cases, where the effect is less pronounced. More recently, KSF have isolated the true source of such numerical errors as being related to inconsistencies between vertical and horizontal advection.

The flow examples in Fig. 13 thus illustrate that the improvement that can be expected from the SLEVE coordinate will vary greatly from case to case and from model to model. It is relevant in this context that the example considered is based on a heavily simplified flow in the absence of parameterized physics and model diffusion, and these latter factors may represent additional sources of small-scale errors.

c. Real-case numerical simulations

Next we consider a real-case numerical experiment motivated by real-time operations of the MC2 during the field phase of the Mesoscale Alpine Programme (MAP; see Bougeault et al. 2001). During this project, the MC2 model was used to produce daily 27-h forecasts with a convection-resolving horizontal grid spacing of 3 km, using a computational mesh with $350 \times 300 \times 50$ grid points covering the entire Alps. A detailed description of the model's setup can be found in Benoit et al. (2002).

The setup of the MC2 for the following experiment is identical to that used during the MAP field phase, except for the use of a digital topography file with higher effective resolution. The currently employed prefiltering of the topography completely removes the shortest wavelength represented, but the smoothing is weaker than that applied during the MAP operations (Benoit et al. 2002) and that typically used in operational NWP models (e.g., SMAP). The comparatively weak filtering is selected to amplify the role of poorly resolved scales, and to demonstrate the ability of the new coordinate to cope with highly complex topography.

The case presented in this section was initialized at 2100 UTC 19 September 1999, and it covers the second day of the MAP Intensive Observing Period (IOP) 2b. The weather situation was characterized by strong southerly flow over the Alps, leading to heavy precipitation and foehn winds upstream and downstream, respectively. Related observational activities during MAP included airborne missions in support of heavy precipitation and gravity wave objectives (Bougeault et al. 2001). Figure 14 shows the simulated fields in a cross section running from west to east across the southern portion of the Alps. The left-hand panels of Fig. 14 depict results of a MAP-like setup using the sigma coordinates (5), while results with the SLEVE coordinate are shown in the right-hand panels. The latter coordinate

transformation is given by (14) with $s_1 = 10$ km and $s_2 = 2$ km ($\gamma = 0.25$). Figures 14a,b depict the computational levels. Results are shown for forecast time $+4$ h, but the results are qualitatively similar at later times. The fields presented include the potential temperature and horizontal velocity in the direction of the cross section (Figs. 14c,d), as well as relative humidity and equivalent potential temperature (Figs. 14e,f). The simulation using the sigma formulation (Figs. 14a,c,e) is characterized by unphysical small-scale variations in virtually all fields, even at upper levels. Some of the associated features show a columnar structure aligned with peaks of the underlying topography, suggesting a numerical, rather than a physical, origin. As discussed above, the noise level in this simulation is at least partly due to the use of a high-resolution topography file. It is likely that several model components contribute toward amplifying small scales, among them the dynamical core, the advection of moisture and cloud species, as well as the parameterization package. In the simulation using the new coordinate formulation (Figs. 14b,d,f), a notable fraction of the unphysical noise is removed as a result of using smoother terrain-following surfaces.

6. Conclusions

The motivation for this study is the recognition that terrain-following coordinate transformations in atmospheric models play an important role in determining the error of numerical algorithms. For analysis, consideration was given to an idealized advection test (section 3), theoretical considerations of the truncation error (section 4), and idealized and real-case numerical experiments using a nonhydrostatic model (section 5). The key results of the study are as follow:

• Theoretical considerations demonstrate that the leading-order truncation error contains not only the well-known error contributions that occur in the presence of a uniform grid, but there is an additional error term of the same order of accuracy that originates from coordinate transformations. The coefficient of the latter error term is associated with horizontal derivatives of the Jacobian. This term dominates in the presence of large-scale flow anomalies, when the regular-grid contribution becomes small.

• Results of the idealized advection test confirm the important role of small-scale terrain features. Using the classical sigma coordinate, the total error may be dominated by transformation rather than regular-grid truncation errors. The former type of error occurs at scales that are relevant for atmospheric prediction models. Taking a 10% error level as a threshold, this level is exceeded for topographic wavelengths smaller than $7-13\Delta x$, depending upon the scheme under consideration.

• Higher-order (e.g., fourth order) advection schemes

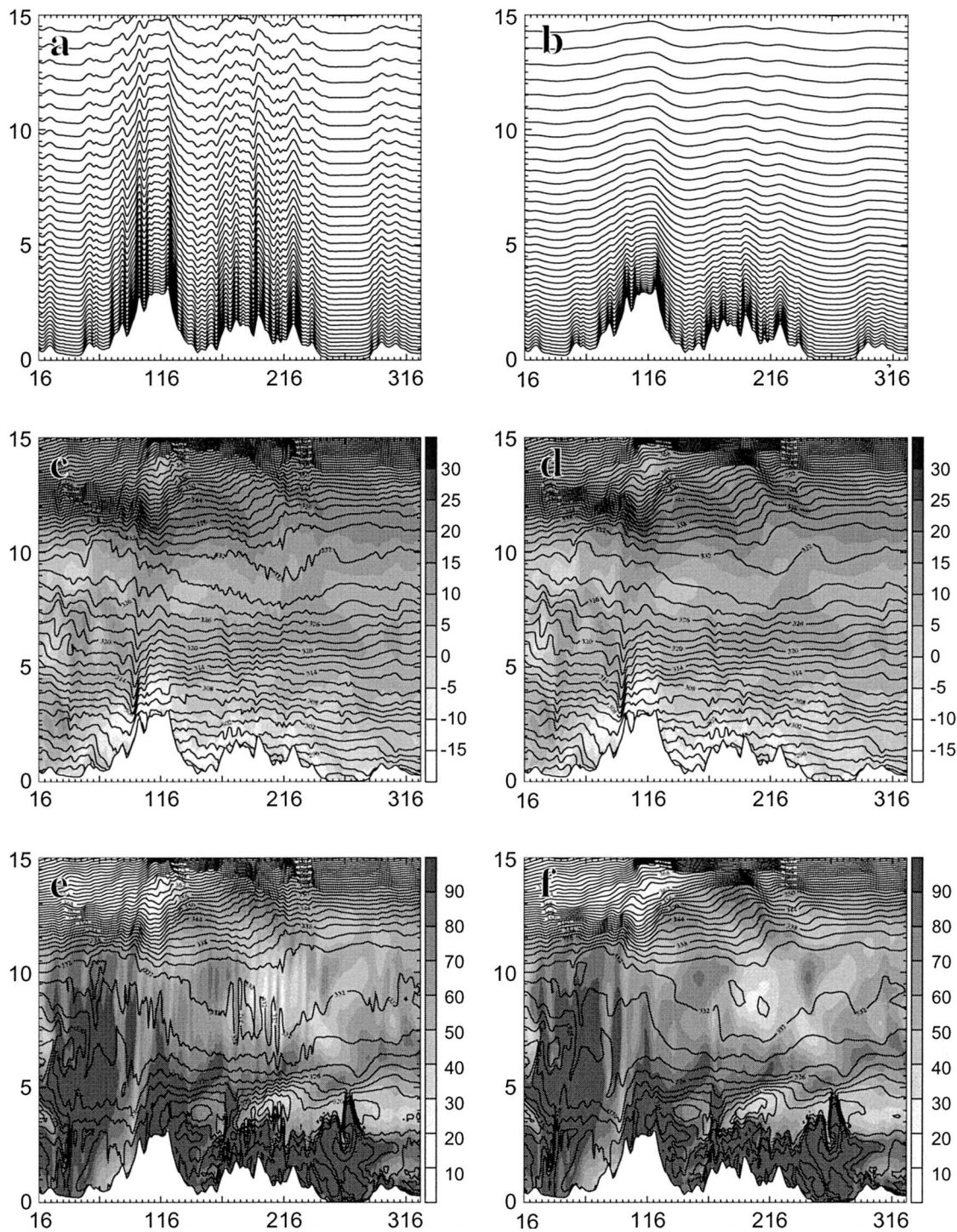FIG. 14. Results of the real-case experiments. Shown is a section across the Alps at 46°N with a horizontal extent of ~930 km (running from west to east from the Rhone valley over the Monte Rosa massif, the Alpine foothills in southern Switzerland, the Po valley in the Veneto area, to the Dinaric Alps in Slovenia). Only the lowermost 15 km of the computational domain are displayed. (a),(b) Heights of computational surfaces, (c),(d) horizontal velocity along the cross section (m s^{-1}) and contours of potential temperature (K), and (e),(f) relative humidity (%) and contours of equivalent potential temperature (K). Left- and right-hand panels show results obtained with the sigma and SLEVE coordinates, respectively.

may not only be attractive for the transport of small-scale anomalies, but they have also a highly beneficial impact if larger-scale anomalies are advected in the presence of small-scale coordinate-transformations.

To alleviate the negative effects of coordinate transformations, a new vertical coordinate framework has been proposed. It is designed to provide a computational mesh that is much smoother than currently utilized coordinate systems (section 2). The basic idea of this new coordinate is the use of a scale-dependent vertical decay of terrain features, such that small-scale variations decay quickly with height so as to leave the coordinate surfaces at midtropospheric and higher levels unaffected. The resulting ''SLEVE'' coordinate yields substantially smoother coordinates than are attainable with a hybrid coordinate. Indeed the splitting of the topography into two (or more) contributions is the key to yielding such a smooth terrain-following coordinate.

The new coordinate formulation has a highly beneficial impact:

- Comparisons of the SLEVE coordinate in the context of the idealized advection test against the performance of sigma and hybrid coordinates demonstrate that the use of a smooth computational grid can greatly reduce the transformation errors and thereby drastically improve the simulation results.
- Idealized and real-case numerical simulations using a full model demonstrate that the new coordinate framework leads to a better representation of gravity waves and reduces the noise levels in the free troposphere and lower stratosphere, although this effect depends upon the model and setup under consideration.

Currently a study is under way to investigate the behavior of the SLEVE coordinate in an operational NWP context using the Lokal Modell (LM; Doms and Schättler 1999) of the German Weather Service. Preliminary results (see Leuenberger 2002) demonstrate that smooth coordinate surfaces indeed help to reduce finescale noise in wind and moisture fields. Leuenberger also demonstrates that the impact depends upon the case under consideration, with particularly evident effects in a case of parameterized summer convection over complex topography. Further analysis will be needed to corroborate this result and to isolate the impact in a larger sample of cases.

When using atmospheric prediction models for real-case applications, there is the desire to represent the underlying topography as accurately as possible. Such a representation does imply some coordinate transformation errors, and a compromise has to be made between accepting these errors or reducing the amplitude of small-scale topographic features. In particular at low levels, it will not be possible to completely remove the associated coordinate transformation errors. As long as they merely affect small-scale atmospheric features (which are anyway poorly resolved), such errors may be acceptable. In contrast, however, such errors are unacceptable when they affect the larger-scale dynamics (which is believed to be well represented). As demonstrated by the theoretical considerations and the idealized numerical tests of this study, the coordinate transformation errors may sometimes represent the dominant error source, and they may greatly be reduced by use of a smooth computational mesh, such as is provided by the SLEVE coordinate.

REFERENCES

Adcroft, A., C. Hill, and J. Marshall, 1997: Representation of topography by shaved cells in a height coordinate ocean model. *Mon. Wea. Rev.,* **125,** 2293–2315.

Benoit, R., M. Desgagné, P. Pellerin, Y. Chartier, and S. Desjardins, 1997: The Canadian MC2: A semi-Lagrangian, semi-implicit wideband atmospheric model suited for finescale process studies and simulation. *Mon. Wea. Rev.,* **125,** 2382–2415.

——, P. Pellerin, N. Kouwen, H. Ritchie, N. Donaldson, P. Joe, and E. D. Soulis, 2000: Toward the use of coupled atmospheric and hydrologic models at regional scale. *Mon. Wea. Rev.,* **128,** 1681–1706.

——, and Coauthors, 2002: The real-time ultrafinescale forecast support during the special observing period of the MAP. *Bull. Amer. Meteor. Soc.,* **83,** 85–109.

Bonaventura, L., 2000: A semi-implicit semi-Lagrangian scheme using the height coordinate for a nonhydrostatic and fully elastic model of atmospheric flows. *J. Comput. Phys.,* **158,** 186–213.

Bougeault, P., P. Binder, A. Buzzi, R. Dirks, R. Houze, J. Kuettner, R. B. Smith, R. Steinacker, and H. Volkert, 2001: The MAP special observing period. *Bull. Amer. Meteor. Soc.,* **82,** 433–462.

Clark, T. L., 1977: A small-scale numerical model using a terrain-following coordinate transformation. *J. Comput. Phys.,* **24,** 186–215.

Davies, L. A., and A. R. Brown, 2001: Assessment of which scales of orography can be credibly resolved in a numerical model. *Quart. J. Roy. Meteor. Soc.,* **127,** 1225–1237.

Doms, G., and U. Schättler, cited 1999: The nonhydrostatic limited-area model LM (Lokal-Modell) of the DWD. Part I: Scientific documentation. German Weather Service (DWD), Offenbach, Germany. [Available from http://www.cosmo-model.org.]

Durran, D. R., 1998: *Numerical Methods for Wave Equations in Geophysical Fluid Dynamics.* Texts in Applied Mathematics, No. 32, Springer, 465 pp.

Egger, J., 1972: Numerical experiments on the cyclogenesis in the Gulf of Genua. *Contrib. Atmos. Phys.,* **45,** 320–346.

Gal-Chen, T., and R. Sommerville, 1975: On the use of a coordinate transformation for the solution of the Navier–Stokes equations. *J. Comput. Phys.,* **17,** 209–228.

Gallus, W. A., and J. B. Klemp, 2000: Behavior of flow over step orography. *Mon. Wea. Rev.,* **128,** 1153–1164.

Janjić, Z. I., 1989: On the pressure gradient force error in σ-coordinate spectral models. *Mon. Wea. Rev.,* **117,** 2285–2292.

Leuenberger, D., 2002: The SLEVE coordinate in LM. *COSMO News-*

letter, No. 2, 104–109. [Available online at http://www.cosmo-model.org.]

Lüthi, D., C. Schär, and H. C. Davies, 1989: On the atmospheric response to steady mesoscale low-level diabatic heating. *Contrib. Atmos. Phys.,* **62,** 126–150.

Mesinger, F., Z. I. Janjić, S. Ničkovic, D. Gavriov, and D. G. Deaven, 1988: The step-mountain coordinate: Model description and performance for cases of Alpine lee cyclogensis and for a case of an Appalachian redevelopment. *Mon. Wea. Rev.,* **116,** 1493–1518.

Phillips, N. A., 1957: A coordinate system having some special advantages for numerical forecasting. *J. Meteor.,* **14,** 184–185.

Pinty, J. P., R. Benoit, E. Richard, and R. Laprise, 1995: Simple tests of a semi-implicit semi-Lagrangian model on 2D mountain wave problems. *Mon. Wea. Rev.,* **123,** 3042–3058.

Simmons, A. J., and D. M. Burridge, 1981: An energy and angular-momentum conserving finite-difference scheme and hybrid vertical coordinates. *Mon. Wea. Rev.,* **109,** 758–766.

Smolarkiewicz, P. K., 1984: A fully multidimensional positive definite advection transport algorithm with small implicit diffusion. *J. Comput. Phys.,* **54,** 325–364.

Steppeler, J., G. Doms, U. Schättler, H. W. Bitzer, A. Gassmann, U. Damrath, and G. Gregoric, 2002: Meso-gamma scale forecasts using the nonhydrostatic model LM. *Meteor. Atmos. Phys.,* in press.

Tanguay, M., A. Robert, and R. Laprise, 1990: A semi-implicit semi-Lagrangian fully compressible regional forecast model. *Mon. Wea. Rev.,* **118,** 1970–1980.

Thomas, S. J., C. Girard, R. Benoit, M. Desgagné, and P. Pellerin, 1998: A new adiabatic kernel for the MC2 model. *Atmos.–Ocean,* **36,** 241–270.

Webster, S., J. Thuburn, B. J. Hoskins, and M. Rodwell, 1999: Further development of a hybrid-isentropic GCM. *Quart. J. Roy. Meteor. Soc.,* **125,** 2305–2331.

Zhu, Z., J. Thuburn, B. J. Hoskins, and P. H. Haynes, 1992: A vertical finite-difference scheme based on a hybrid σ–θ–p coordinate. *Mon. Wea. Rev.,* **120,** 851–862.